


## Article

# A Novel Method for the Preparation of Fibrous $\text{CeO}_2\text{-ZrO}_2\text{-Y}_2\text{O}_3$ Compacts for Thermochemical Cycles

Nicole Knoblauch \* and Peter Mechnich 

German Aerospace Center (DLR), Institute of Materials Research, 51147 Köln, Germany; Peter.Mechnich@dlr.de

\* Correspondence: Nicole.Knoblauch@dlr.de

**Abstract:** Zirconium-Yttrium-co-doped ceria ( $\text{Ce}_{0.85}\text{Zr}_{0.13}\text{Y}_{0.02}\text{O}_{1.99}$ ) compacts consisting of fibers with diameters in the range of 8–10  $\mu\text{m}$  have been successfully prepared by direct infiltration of commercial YSZ fibers with a cerium oxide matrix and subsequent sintering. The resulting chemically homogeneous fiber-compacts are sinter-resistant up to 1923 K and retain a high porosity of around 58 vol% and a permeability of  $1.6\text{--}3.3 \times 10^{-10} \text{ m}^2$  at a pressure gradient of 100–500 kPa. The fiber-compacts show a high potential for the application in thermochemical redox cycling due to its fast redox kinetics. The first evaluation of redox kinetics shows that the relaxation time of oxidation is five times faster than that of dense samples of the same composition. The improved gas exchange due to the high porosity also allows higher reduction rates, which enable higher hydrogen yields in thermochemical water-splitting redox cycles. The presented cost-effective fiber-compact preparation method is considered very promising for manufacturing large-scale functional components for solar-thermal high-temperature reactors.



**Citation:** Knoblauch, N.; Mechnich, P. A Novel Method for the Preparation of Fibrous  $\text{CeO}_2\text{-ZrO}_2\text{-Y}_2\text{O}_3$  Compacts for Thermochemical Cycles. *Crystals* **2021**, *11*, 885. <https://doi.org/10.3390/cryst11080885>

Academic Editors: Maged Bekheet and Ulla Simon

Received: 29 June 2021

Accepted: 26 July 2021

Published: 29 July 2021

**Publisher's Note:** MDPI stays neutral with regard to jurisdictional claims in published maps and institutional affiliations.

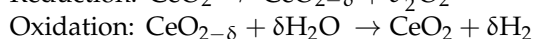
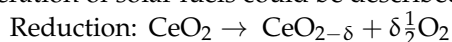


**Copyright:** © 2021 by the authors. Licensee MDPI, Basel, Switzerland. This article is an open access article distributed under the terms and conditions of the Creative Commons Attribution (CC BY) license (<https://creativecommons.org/licenses/by/4.0/>).

**Keywords:** Zirconium-Yttrium-co-doped ceria; fiber-compact; thermochemical redox cycling

## 1. Introduction

Solar energy in combination with redox materials can be utilized for thermochemical dissociation of water. Ceria is a very promising material for this process due to its redox thermodynamics and fast redox kinetics, e.g., [1–6]. If ceria is used as redox material the generation of solar fuels could be described as follows:



Doping ceria with tetravalent cations like  $\text{Zr}^{4+}$  is promising in terms of enhanced oxygen release during reduction [7–13]. The solubility of  $\text{Zr}^{4+}$  in cubic ceria is given up to ~20 mol%, only at higher  $\text{Zr}^{4+}$  concentrations tetragonal Zr-rich phases [9,14–16], which have a lower oxygen storage capacity, can be formed. Investigations on oxygen release indicate that the degree of reduction increases with increasing  $\text{Zr}^{4+}$  concentration up to 15–25 mol% [8,13,17]. The improvement is often attributed to the smaller ionic radius of  $\text{Zr}^{4+}$ , which compensates stresses due to volume changes in the lattice caused by the larger  $\text{Ce}^{3+}$  ions [18–20]. In addition, the smaller  $\text{Zr}^{4+}$  ion prefers a seven-fold coordination with oxygen in contrast to the eight-fold coordination as in the  $\text{CaF}_2$  (fluorite) structure, which facilitates the formation of oxygen vacancies by reduction of  $\text{Ce}^{4+}$  to  $\text{Ce}^{3+}$  [9,21–23]. Therefore, the oxygen vacancies are preferably located next to the zirconium ions, which leads to pyrochlore arrangements [10,24]. Besides the improved reduction behavior, the oxidation kinetics and the reoxidation with  $\text{H}_2\text{O}$  is slowed down with increasing  $\text{Zr}^{4+}$  concentration compared to undoped ceria [13,17,25]. As causes for the worsened reoxidation, in addition to the changed thermodynamic properties [9,10,24,26], the slowed kinetics due to sintering which results in longer diffusion paths and a smaller specific surface area, are discussed [27–29]. Studies by Scheffe et al. [13] show that an increase in the reactive surface area has a positive effect on the reoxidation. Furthermore, a co-doping

with trivalent cations could be promising. Doping ceria-zirconia with trivalent oxides like  $\text{Y}_2\text{O}_3$  leads to a stabilization of the cubic structure and suppression of degradation effects [30,31]. Additionally, trivalent cations induce formation of further oxygen vacancies in the fluorite structure, which increases the oxygen ion mobility [32,33]. These further oxygen vacancies could affect the interaction of  $\text{Zr}^{4+}$  and oxygen vacancies built during reduction of  $\text{Ce}^{4+}$  to  $\text{Ce}^{3+}$  [34].

Our incentive was to combine high sinter-resistant porosity with trivalent doping to achieve the best possible redox performance for  $\text{Zr}^{4+}$  doped ceria. With regard to porous shaped bodies, a number of things have already been described in the literature. Pullar et al. [35] reports on fibrous, three dimensionally ordered macroporous, reticulated and biomimetic porous ceria materials. Porous ceria felt, made from a sheet of compressed commercial ceria fibers, has been already investigated using simulated concentrated solar light by Furler et al. [36,37]. In these studies, the production rates of the felts were very low due to the low rate of heat transfer. Furthermore, the concentrated solar light was found to destroy the fibrous structure [38]. Another study of commercial fibrous ceria particles described by Gladen and Davidson [39] and tested for  $\text{CO}_2$  splitting reach low CO yields of only  $1.15 \text{ mL g}^{-1}$  which is in combination with the high cost of these fibers and, therefore, makes them less valuable. The fibers of Gibbons et al. [40] prepared by electrospinning with a favored  $\text{Zr}^{4+}$  doping level of 2.5 mol%, initially show a high CO production of  $3.9 \text{ mL g}^{-1}$ , but a continuous increase in the reduction temperature was also observed, indicating further sintering of the fibrous compact. However, with a higher resistance against sintering effects, much greater overall yields by higher  $\text{Zr}^{4+}$  doping and fast oxidation kinetics by further three valent doping, a fibrous compact could be very promising for thermochemical cycling.

In this work we present a novel, cost-effective, facile direct processing method for fibrous highly porous Ce-oxide ceramics. Reaction sintering of Ce-oxide and added chopped yttria-stabilized zirconia (YSZ) fibers provides co-doped ceria  $\text{Ce}_{0.85}\text{Zr}_{0.13}\text{Y}_{0.02}\text{O}_{1.99}$  compacts with sinter-resistant fibrous microstructure. Furthermore, the influence of temperature on doping element distribution, microstructure and porosity are discussed in view of the applicability as redox material to be used in cyclic thermochemical processes.

## 2. Materials and Methods

### 2.1. Sample Preparation

YSZ fiber felts (5mol%  $\text{Y}_2\text{O}_3$ , ZYF, Zircar Zirconia Inc., Florida, NY, USA) were disintegrated into individual short fiber fragments of 20–200  $\mu\text{m}$  by means of high-energy agitation in a resonant acoustic mixer (LabRAM II, Resodyn mixers Inc., Butte, MT, USA). The RAM device was also employed to prepare aqueous slurries consisting of YSZ fibers and  $\text{CeO}_2$  nanopowders (70–105 nm, ChemPur, Germany) in the required mol fraction ( $\text{CeO}_2$ : YSZ:  $\text{H}_2\text{O}$ ; 85:15:17). A carbonic acid salt (Dolapix PC80 164413, Zschimmer & Schwarz, Germany) was used as dispersant (4 drops per 10 mL  $\text{H}_2\text{O}$ ). The aqueous slurry was then filled into a flexible, disc-shaped silicone mold and allowed to dry slowly at ambient temperature. For comparison,  $\text{CeO}_2$  nanopowders and YSZ nanopowders (5.4vol%  $\text{Y}_2\text{O}_3$ , PlasmaChem GmbH, Germany) were dry mixed and pressed into pellets. Samples were subsequently sintered at temperatures between 1573 K and 1923 K (10K/min) for 2 h under ambient air.

### 2.2. Sample Characterization

The sintered samples were characterized by scanning electron microscopy (DSM Ultra 55 FEG, Carl Zeiss, Germany) and energy-dispersive X-ray spectroscopy (EDS, INCA, Oxford Instruments, Abingdon, UK). X-ray powder diffraction (XRD, D8 Advanced, Bruker AXS, Karlsruhe, Germany) using  $\text{Cu-K}\alpha$  radiation and EVA/TOPAS software package was used for phase analyses. A Pt-strip-heated stage was also employed for in-situ high-temperature XRD under ambient air (HTK 16N, Anton-Paar, Graz, Austria). In order to

obtain maximum intensity at fast scan rates, experiments were performed without Ni primary filter.

The helium pycnometer (AccuPyc® II 1340, Micromeritics, GA, USA) was used to determine the skeletal density of the porous compounds by means of gas displacement. In addition, the enveloping density was determined using a sand pycnometer (Geopyc 1360, Micromeritics, GA, USA). The principle of volume displacement was applied with the aid of Dry Flo, a solid medium. Together with the skeletal density the porosity was then calculated.

Furthermore temperature-dependent dimensional changes of samples were recorded by heating microscopy (L74/HS/1600, Linseis, Selb, Germany).

### 2.3. Gas Permeability Test

The air permeability of the porous ceramics was determined by using a custom setup (see sketch in Figure 1). The porous pellet samples with ~2 mm thickness and ~14 mm diameter were carefully embedded in highly viscous epoxy resin in order to avoid any sealing of porosity. Epoxy discs with central samples were fixed in the steel sample holder with the help of two rubber washers. The static air pressure was measured in the front of the sample by pressure transducer whereas the volumetric air flow  $Q$  was measured using a standard laboratory rotameter installed downstream.

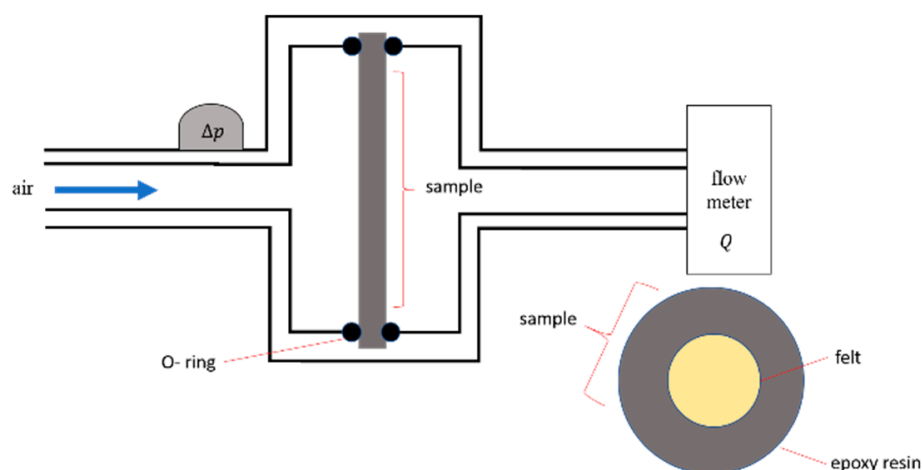


**Figure 1.** Permeability setup for porous pellet samples.

### 2.4. Evaluation of Redox Kinetics

For the evaluation of redox kinetics thermogravimetric analyses (STA 449 F3 Jupiter, Netzsch, Selb, Germany) were performed on samples of  $\text{Ce}_{0.85}\text{Zr}_{0.13}\text{Y}_{0.02}\text{O}_{1.99}$  pre-treated at different temperatures in order to determine equilibrium oxygen vacancy concentrations  $\delta(\text{pO}_2, T)$ . For reduction the samples were heated by a ramp of 20 K/min under Ar (purity of 99,999%, 85 mL/min) and held for 2 h at high temperature. Afterward the samples were cooled down by 50 K/min under argon to the required oxidation temperature and then reoxidized with an oxygen (17 mL/min) / argon (68 mL/min) mixture for 30 min. The concentration of oxygen in the TGA was also controlled and measured using a Nernst-type oxygen detector (GEN'AIR, Setnag, Marseille, France).

## 3. Results and Discussion

### 3.1. Fabrication and Microstructural Evolution of Fibrous Y,Zr Co-Doped $\text{CeO}_2$ Compacts

The microstructures of the used YSZ fiber are shown in Figure 2. The close-up of the fiber reveals a curled surface and very fine grains in the nanometer range.

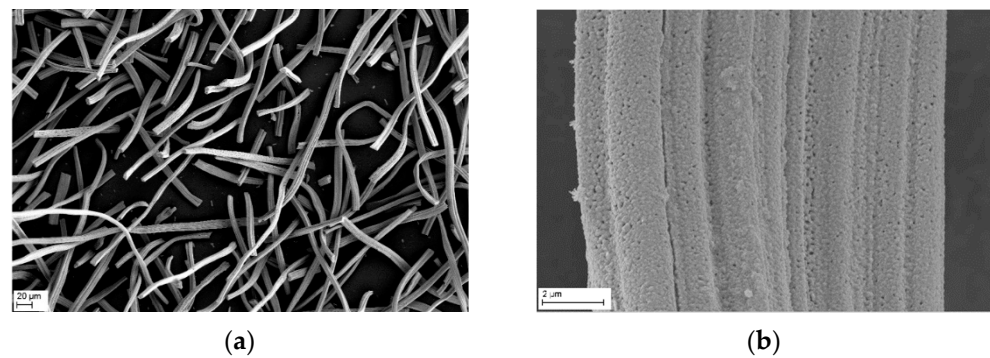


**Figure 2.** SEM micrographs of YSZ felt before thermal treatment in different magnification (a,b).

After thermal treatment at a high temperature of 1923 K the grains grew up to 2  $\mu\text{m}$ –8  $\mu\text{m}$  whereas the diameter of the fiber remained or shrank (Figure 3a).

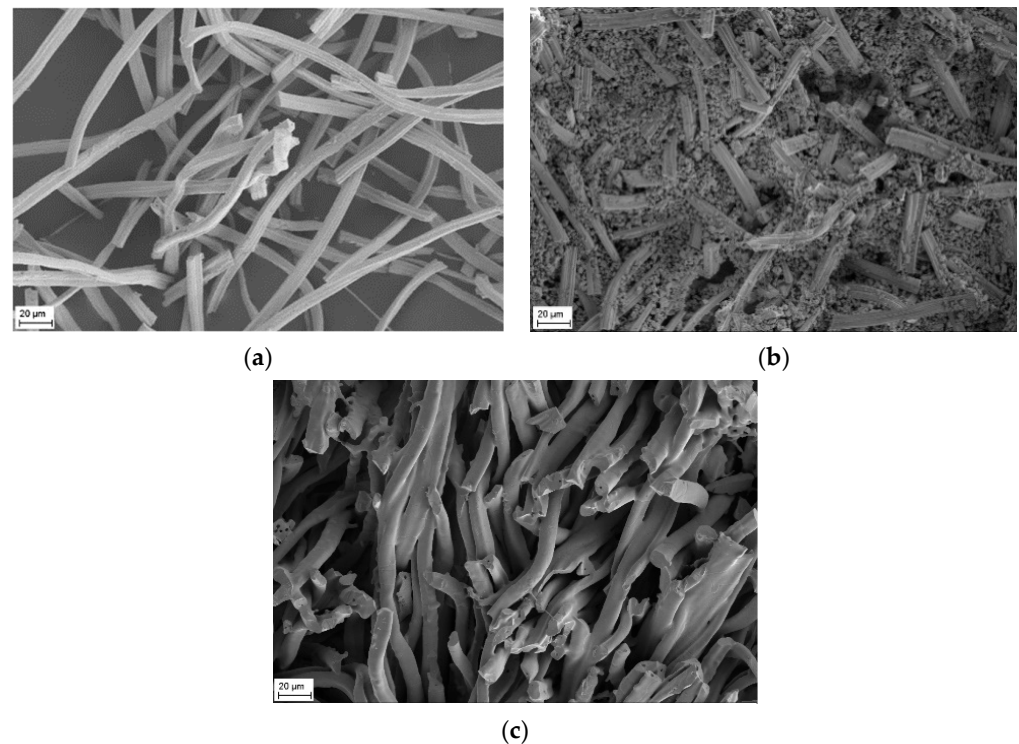


**Figure 3.** SEM micrographs of pure YSZ fiber after thermal treatment at 1923 K for 2 h (a) and SEM micrographs of YSZ fiber mixed with  $\text{CeO}_2$  after thermal treatment at 1573 K (b) and 1923 K (c).

For the preparation of fibrous  $\text{CeO}_2\text{-ZrO}_2\text{-Y}_2\text{O}_3$  compacts the shopped YSZ fibers of Figure 2 were mixed with  $\text{CeO}_2$  as described previously. After a temperature treatment at 1573 K, a small amount of  $\text{CeO}_2$  has already diffused into the YSZ fiber, according to the results of SEM in Figure 3b and peak shift of diffraction in Figure 4a. However, the majority of cerium oxide is still present as a matrix next to the fibers, as seen in Figure 3b. As the temperature increases, the matrix content decreases significantly. After a temperature treatment at 1923 K, the cerium oxide matrix has almost disappeared (Figure 3c).

Figure 3 also enables a comparison between stand-alone YSZ fibers and reacted fibers after reaction at 1923 K (Figure 3a,c), respectively. It is evident that fibers in the former  $\text{CeO}_2/\text{YSZ}$  mixture now have a significantly greater diameter and grain morphology is quite different to the ‘bamboo’-like morphology of stand-alone YSZ fibers. The only plausible effect explaining the observed microstructure and chemical composition is massive diffusion of  $\text{CeO}_2$  into YSZ fibers and subsequent formation of the new phase. According

to the results of EDS and X-ray diffraction (Figure 4) the phase could be described as  $\text{Ce}_{0.85}\text{Zr}_{0.13}\text{Y}_{0.02}\text{O}_{1.99}$  solid solution.

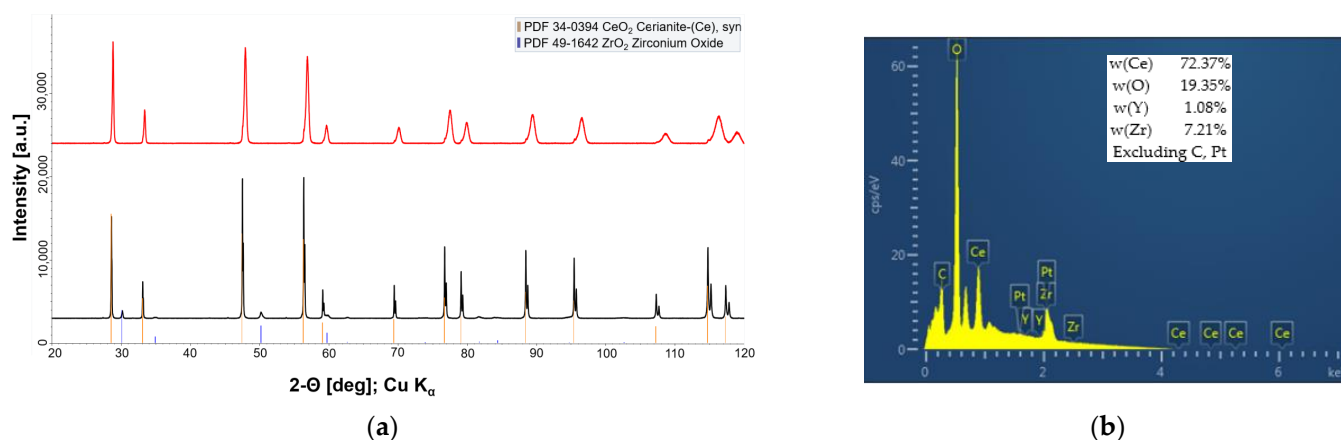


**Figure 4.** (a) XRD-profile of the  $\text{CeO}_2/\text{YSZ}$  felt mixture after heat treatment at 1573 K (black) and 1923 K (red). (b) EDS results of the  $\text{CeO}_2/\text{YSZ}$  felt mixture after heat treatment at 1923 K.

‘Swelling’ fibers, i.e., increasing fiber volume and the simultaneously disappearing  $\text{CeO}_2$  space filling raised the question if volumetric effects could also be associated with this specific reaction. Actually, such volume effects associated with  $\text{CeO}_2$ -diffusion into YSZ fibers at higher temperatures could also be observed directly via the change in sample dimensions using a heating microscope. Figure 5 shows the relative change according to Equation (1) for pellet samples of pure ceria and ceria with fibers.

$$\frac{\Delta l}{l} = \frac{(L_{\text{CeO}_2-\delta}(\text{T}) - L_{\text{CeO}_2}(\text{T}))}{L_{\text{CeO}_2}(\text{T})} \quad (1)$$

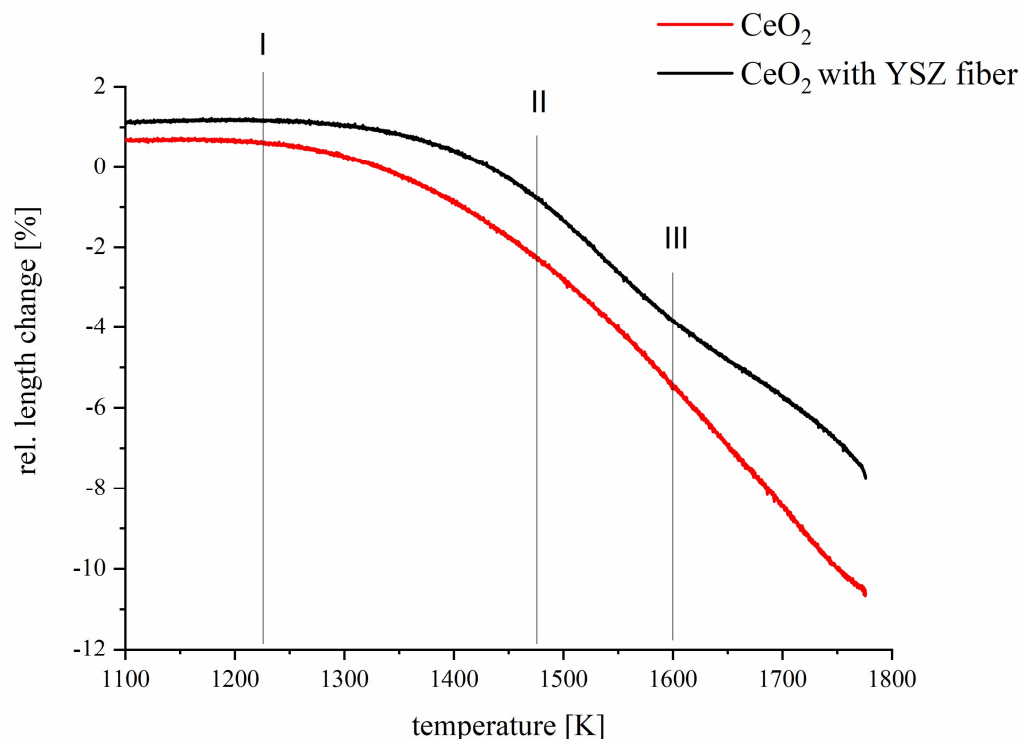


**Figure 5.** The relative length changes of sample dimension of  $\text{CeO}_2$  (red) and  $\text{CeO}_2$  with YSZ fiber (black) as function of temperature.



$\Delta l$  = length change,  $L$  = length of the sample,  $L_{\text{CeO}_2-\delta}$  = length of the heated and maybe reduced sample,  $L_{\text{CeO}_2}(T)$  = length of the oxidized sample at 293K.

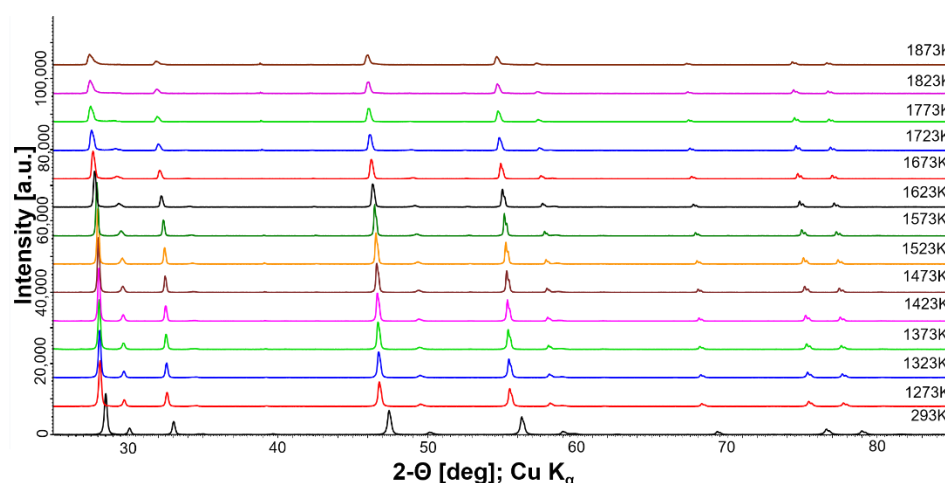
The curve shape of pure ceria (Figure 5, red curve) corresponds to the expected temperature-induced shrinkage linked to volume and grain boundary diffusion processes. The onset temperature of sinter-shrinkage is appr. 1150 K, then the sintering curve exhibits a conventional parabolic shape. In contrast, the respective sintering curve of  $\text{CeO}_2/\text{YSZ}_f$  (Figure 5, black curve) shows three significantly differing features. The onset temperature for sintering is appr. 1250 K (I). A slight deviation from the parabolic shape is observed at about 1450 K, where sintering seems to accelerate (II). Interestingly, the sintering significantly slows down again above 1600 K as seen by the curve trending to a lower relative length change (III). As thermal activation for sintering is expected to be similar for both samples, there is obviously a kind of superposed volume expansion effect in the case of the  $\text{CeO}_2/\text{YSZ}_f$  sample. This expansion could indicate a just-beginning reduction of  $\text{Ce}^{4+}$  to  $\text{Ce}^{3+}$  that could be accompanied by an expansion of the crystal lattice [41]. According to the literature,  $\text{Zr}^{4+}$  addition decreases the temperature of the reduction step compared to pure ceria [16], which could explain the observed effect. However, it is concluded that the significant dilatometer curve is most likely due to in-diffusion of  $\text{CeO}_2$  into the rigid YSZ fiber network and subsequent ‘swelling’ due to formation of the assumed new solid solution. The fact that  $\text{CeO}_2/\text{YSZ}_f$  retains its fibrous morphology and shows much less sinter-shrinkage than conventional  $\text{CeO}_2$  powder compacts is considered a unique feature for manufacturing and operation of porous bodies at extremely high temperatures.

The observed, nearly complete diffusion of  $\text{CeO}_2$  into the YSZ fiber network was an a priori unexpected behavior which motivated us for deeper analysis of underlying mechanisms. Besides SEM, EDS and heating microscope, the reaction between  $\text{CeO}_2$  powders and YSZ fibers was monitored in situ by HT-XRD between 1273 K and 1873 K. In order to duplicate the standard 10/K min heating profiles used for sample preparation and other analyses, XRD profiles were collected under isothermal conditions combined with faster heating ramps (100 K/min rate).

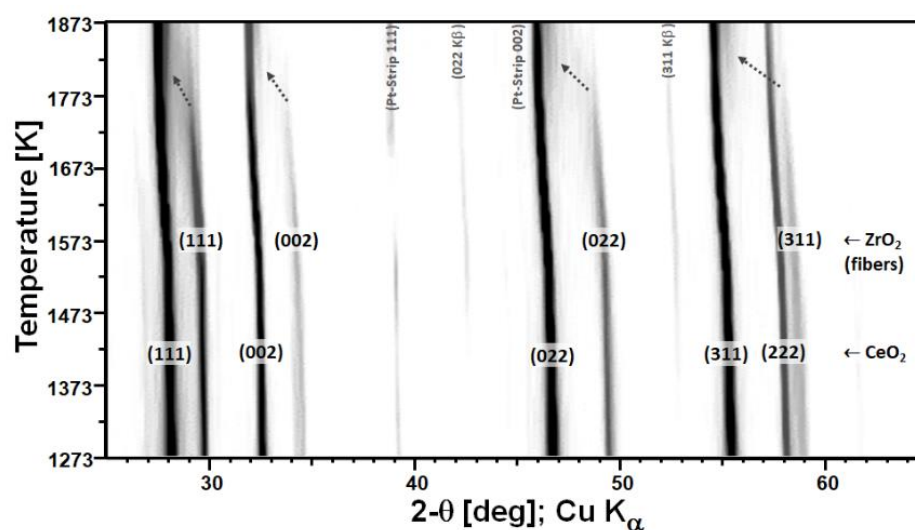
Figure 6a shows a standard ‘stack’ representation of the HTXRD measurements of the  $\text{CeO}_2/\text{YSZ}$  felt mixture. The corresponding ‘plane view’ 2D XRD-profile (Figure 6b) is well suited to display the deviation from standard linear expansion above 1573 K;  $\text{CeO}_2$  as well as YSZ peaks shift significantly faster toward lower 2-theta, whereas the streak of 111 Pt reflection from the sample holder is still linear. Note that weak peaks at 2-theta positions of 43 and 53 are  $K_\beta$  reflections of  $\text{CeO}_2$  caused by insufficient electronic filtering. A remarkable effect is observed for YSZ reflections above 1725 K; in addition to accelerated shifting toward corresponding  $\text{CeO}_2$  peak positions, peaks are fading out and now appear only as ‘shoulders’ of  $\text{CeO}_2$  peaks (see arrows in Figure 6b). This finding is also confirmed by respective lattice constant calculations which were performed by means of analytical profile fitting using the TOPAS software package (see Figure 7). Whereas  $\text{CeO}_2$  only shows a minor decreasing trend above 1573 K, YSZ displays a strong increase above 1725 K and evidently approach  $\text{CeO}_2$  lattice parameters. Evidently, the major impact of cation (inter-)diffusion is occurring in YSZ, and the composition of the newly forming solid solution is evolving in the direction of  $\text{CeO}_2$ . Therefore, it can be concluded that  $\text{CeO}_2$  is diffusing much faster, quasi unidirectionally into YSZ fibers, which also explains the observed microstructure. The schematic diagram in Figure 8 illustrates the observed unusual unidirectional diffusion and the resulting swelling of the YSZ fiber.

In order to study the reaction between  $\text{CeO}_2$  and YSZ fibers we conducted an experiment where fibers were not infiltrated but brought into contact with a similar  $\text{CeO}_2$ -matrix as diffusion couple. For this, a highly viscous  $\text{CeO}_2$  slurry (‘paste’) was prepared wherein a piece of YSZ felt was carefully placed. Due to the high viscosity, undesired infiltration of  $\text{CeO}_2$  into the YSZ felt could be minimized. After thermal treatment (1923 K/2 h) the felt/matrix diffusion couple was stabilized with epoxy resin and prepared for an SEM/EDS analyses. Figure 9 shows the respective cross-section with an approximately 100  $\mu\text{m}$  thick part of the  $\text{CeO}_2$ -matrix on the left. EDS analyses were performed as vertical line scans

across the entire field of view, as indicated by dashed lines. Site-dependent quantifications for Ce, Zr, and Y are plotted as overlay on the SEM image (note that values are normalized to cations). At a glance, concentration profiles of Ce and Zr show a significant deviation from an expected symmetric, sigmoidal shape when entering the  $\text{CeO}_2$ -section of the diffusion couple. Normally, one would initially expect bidirectional (inter-)diffusion of cations. The high-temperature polymorph of YSZ is cubic and isomorphic with  $\text{CeO}_2$ , both being members of the  $\text{AO}_2$  oxides fluorite-type crystal structure family.  $\text{Zr}^{4+}$  is isovalent with  $\text{Ce}^{4+}$  and the effective ionic radii of  $\text{Zr}^{4+}$  and  $\text{Y}^{3+}$  in eight-fold coordination ( $\text{Zr}^{4+} = 84$  pm,  $\text{Y}^{3+} = 102$  pm) are close to the ionic radius of  $\text{Ce}^{4+}$  ( $\text{Ce}^{4+} = 97$  pm) [18], so a diffusion of  $\text{ZrO}_2$  and  $\text{Y}_2\text{O}_3$  into  $\text{CeO}_2$  with some formation of oxygen vacancies to equilibrate charge deficit by  $\text{Y}^{3+}$  ('defect fluorite') seems to be plausible. However, the non-sigmoidal EDS profiles show that the  $\text{Zr}^{4+}$  ion concentration in ceria is relatively low and  $\text{Y}^{3+}$  diffusion into the  $\text{CeO}_2$  matrix is below detectability limits of EDS (see Figure 9). In contrast to these findings, diffusion of  $\text{CeO}_2$  into the YSZ fibers follows the expected trend, as indicated by the parabolic concentration curve.



(a)



(b)

**Figure 6.** (a) Stacked XRD-profiles of the  $\text{CeO}_2$ /YSZ felt mixture at temperatures between 293 K and 1873 K. (b) 'Plane view' (2D) XRD-profile. The arrows illustrate the shift of the peaks of YSZ.

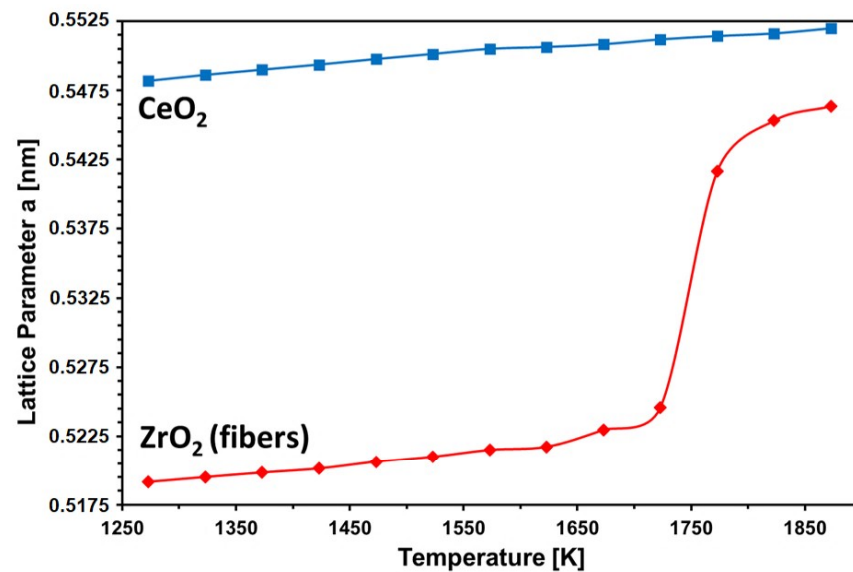


Figure 7. Lattice constant calculation of CeO<sub>2</sub> and YSZ as function of temperature.

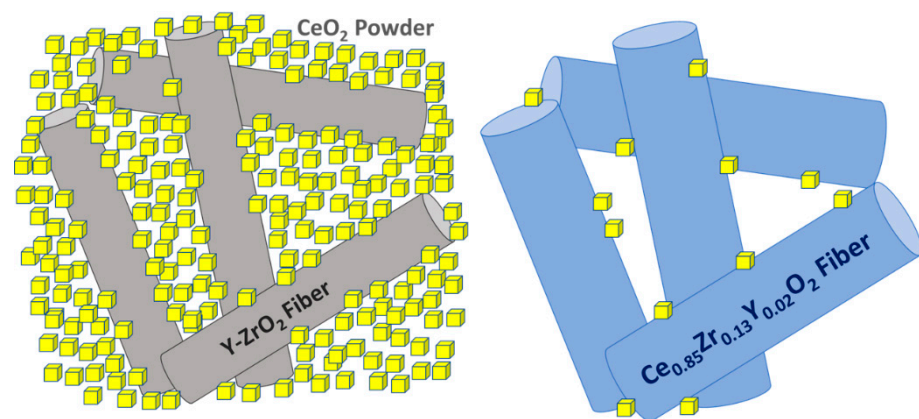
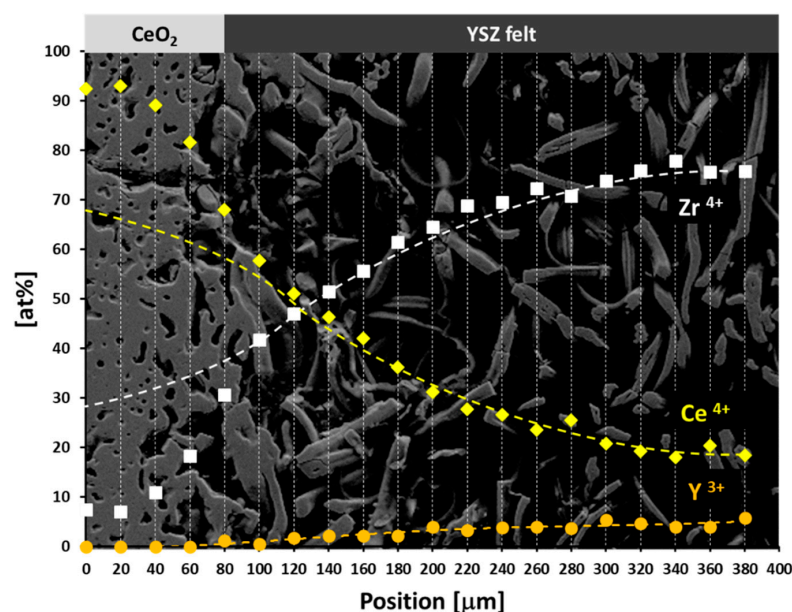


Figure 8. Schematic representation of the matrix fiber interaction after 1573 K and 1923 K.

In general, the diffusion in solids occurs by migration across vacancies and interstitial sites, but not by direct site change mechanism [42]. Grain boundaries, phase boundaries and surfaces are areas with reduced binding energy, which means that surface-diffusion is considerably faster than volume-diffusion [42]. The YSZ of the fibers has a grain size of about 70 nm which is close to the grain size of the used ceria powder. As a result, it is expected that cation diffusion is not due to the difference in grain size but mainly explained by cation vacancies. A vacancy migration controlled cation diffusion in undoped and doped ceria has also been reported by Beschnitt and De Souza [43]. In the case of an acceptor doped system with  $[Y_{Zr}] = 2[V_{O..}]$ , an increasing concentration of the acceptor dopant at constant temperature leads to an decrease of the concentration of  $V_{Zr}'''$ . According to the Schottky equilibrium, the concentration of cation vacancies is inversely proportional to the concentration of oxygen vacancies. Consequently, the bulk cation diffusion coefficient should decrease with increasing  $Y^{3+}$  concentration. Our data, however, shows an opposite trend (Figure 9); cation diffusion seemed to be higher at the high dopant concentration side (Y-doped ZrO<sub>2</sub>) and lower at the undoped ceria side. Such surprising cation diffusion behavior was also observed by Beschnitt and De Souza [43] for  $Zr^{4+}$  diffusion in  $Y^{3+}$ -doped ceria. In the present case, cation diffusion seems to follow a sigmoidal trend in ceria and a parabolic trend in YSZ (see Figure 9).





**Figure 9.** SEM cross-section of a  $\text{CeO}_2$  powder compact/YSZ felt diffusion couple after thermal treatment at 1923 K with superposed EDS quantification data of line scans indicated by dashed lines.

After complete cation diffusion at high temperature, a quasi-homogeneous ceramic with outstanding porosity was formed (Figure 10). Such highly porous and fibrous  $\text{CeO}_2$ - $\text{ZrO}_2$ - $\text{Y}_2\text{O}_3$  ceramics can hardly be obtained by means of sintering of conventional powder mixtures, in particular, at sintering temperatures of 1923 K. This novel preparation also provides advantages in comparison to elaborate the electrospinning process, e.g., [44]. The direct introduction of YSZ fiber into porous ceramics has so far been reported in the literature mainly only in the field of fiber reinforcing porous ceramic, e.g., [45], where the matrix is still present also after the sintering process. In the literature, the highest porosity of porous YSZ ceramics produced via common gel-casting method was 75.9% (after 1623 K for 2 h), but the porosity quickly drops to 66% at higher temperature of 1773 K [46]. Dong et al. obtained with their fabrication method for YSZ ceramics, including YSZ fiber with 10 vol% solid loading and 20 wt% fiber addition, a porosity of 75.4% (sintered at 1773 K for 2 h) [45]. In this study, the porosity of the high sintered  $\text{Ce}_{0.85}\text{Zr}_{0.13}\text{Y}_{0.02}\text{O}_{1.99}$  felt was determined by means of helium pycnometry. The solid density referring to the fibrous oxide was calculated to  $7.05 \pm 0.02 \text{ g/cm}^3$ , i.e., close to the theoretical density of  $\text{CeO}_2$ , indicating a pore-free ‘skeleton’. The bulk density was calculated to  $2.96 \pm 0.14 \text{ g/cm}^3$  which translates to 58 vol% open porosity after sintering at 1923 K.

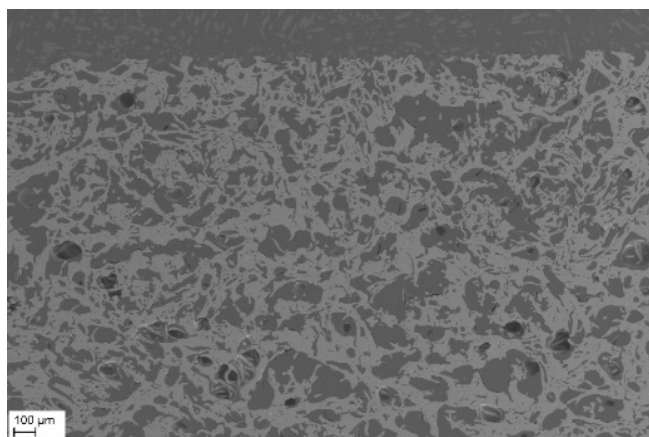


**Figure 10.** SEM cross-section of a  $\text{Ce}_{0.85}\text{Zr}_{0.13}\text{Y}_{0.02}\text{O}_{1.99}$  felt after 1923 K (2 h).

Despite the high sintering temperature, the high porosity of the ceramic body is retained. The fibrous microstructure seems to be very helpful to impede densification during the sintering process. The high porosity enables a high gas permeability. The gas flow through a porous medium is usually described by Darcy's law [47]:

$$K = \frac{Q \cdot \mu \cdot l}{A \cdot \Delta p} \quad (2)$$

where  $K$  = permeability;  $Q$  = flow rate;  $\mu$  = Viscosity coefficient of air;  $l$  = length of the porous body;  $A$  = cross-sectional area of the porous body;  $\Delta p$  = pressure gradient.

Darcy's law indicates that the flow rate through a porous medium is proportional to the pressure gradient  $\Delta p$  and the permeability  $K$  is inversely proportional to the viscosity coefficient  $\mu$  of the gas [48]. Figure 11 depicts the permeability of air through fibrous  $\text{Ce}_{0.85}\text{Zr}_{0.13}\text{Y}_{0.02}\text{O}_{1.99}$  as a function of the pressure gradient  $\Delta p$ .

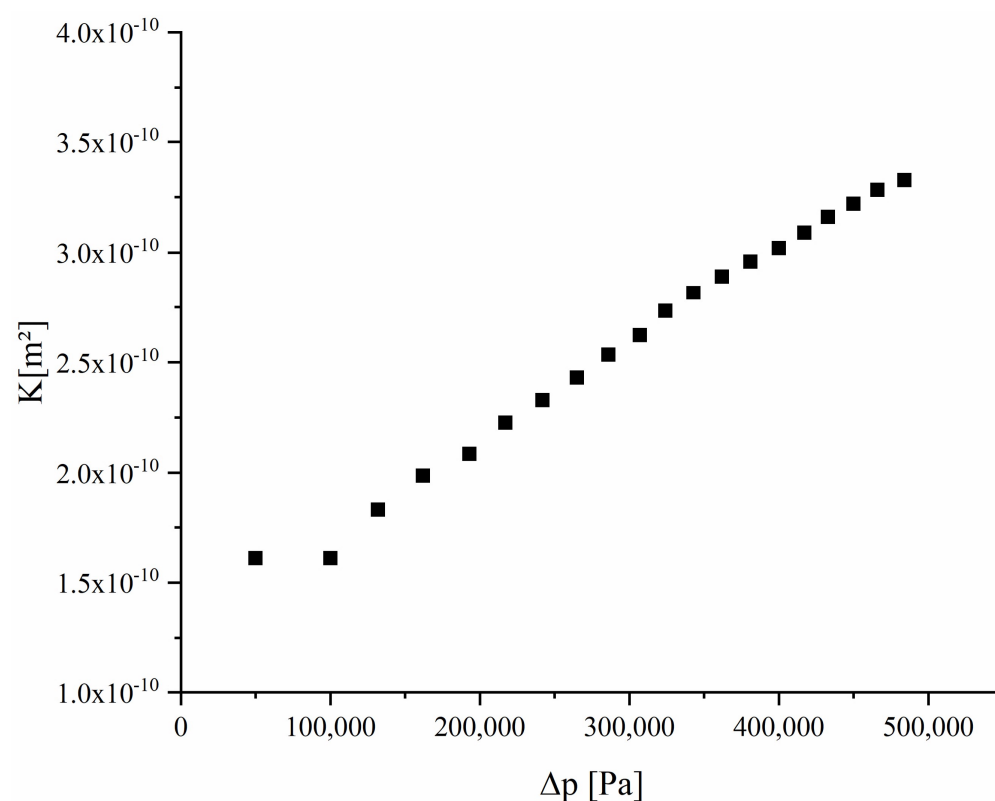


**Figure 11.** The flow rate of air through the porous  $\text{Ce}_{0.85}\text{Zr}_{0.13}\text{Y}_{0.02}\text{O}_{1.99}$  felt as function of the pressure gradient.

A laminar flow as described by Darcy's law can be observed from a pressure gradient of 100,000 Pa. At smaller pressure gradients, the dominating surface forces cause turbulent flow which is responsible for the nonlinear permeability/pressure relationship. The permeability at a higher pressure gradient amounts to values in a range of  $1.6\text{--}3.3 \times 10^{-10} \text{ m}^2$ , close to the values achieved by Haussener and Steinfeld [49] for porous ceria using graphite as the pore former. In comparison to Isobe et al. [50], when achieving permeabilities for nitrogen in the range of  $10\text{--}14 \text{ m}^2$  for porous  $\text{Al}_2\text{O}_3$  samples with unidirectionally aligned pores, our observed permeability values are one to two orders higher.

### 3.2. Redox-Kinetics

The gas permeability is a key to fast redox kinetics for thermochemical cycling. The porosity has a direct influence on the oxygen partial pressure and the related redox kinetics as well as on the hydrogen generation during oxidation due to the higher surface area. To

evaluate the redox performance the oxygen loss  $\delta$  during reduction at high temperature is calculated. The value of  $\delta$  can be determined from the mass changes  $\Delta m$  detected by TGA using the formula:

$$\delta = \frac{M \cdot \Delta m}{M_O \cdot m_s} \quad (3)$$

where  $M$  is the molar mass of  $\text{Ce}_{0.85}\text{Zr}_{0.13}\text{Y}_{0.02}\text{O}_{1.99}$ ,  $\Delta m$  the equilibrium value of the mass change during the redox-reaction,  $m_s$  the sample mass in the fully oxidized state, and  $M_O$  the molar mass of oxygen. Figure 12 shows the  $\delta$  values calculated from the mass loss curves of TGA experiments. Samples are oxidized in air at 1073 K followed by heating to the targeted reduction temperature steps under streaming Ar (purity of 99,999%), respectively. The achieved  $\delta$  values of fibrous  $\text{Ce}_{0.85}\text{Zr}_{0.13}\text{Y}_{0.02}\text{O}_{1.99}$  are comparable to the values of reference monolithic Zr-doped cerium oxide. Compared to pure cerium oxide, significantly higher delta values are observed.

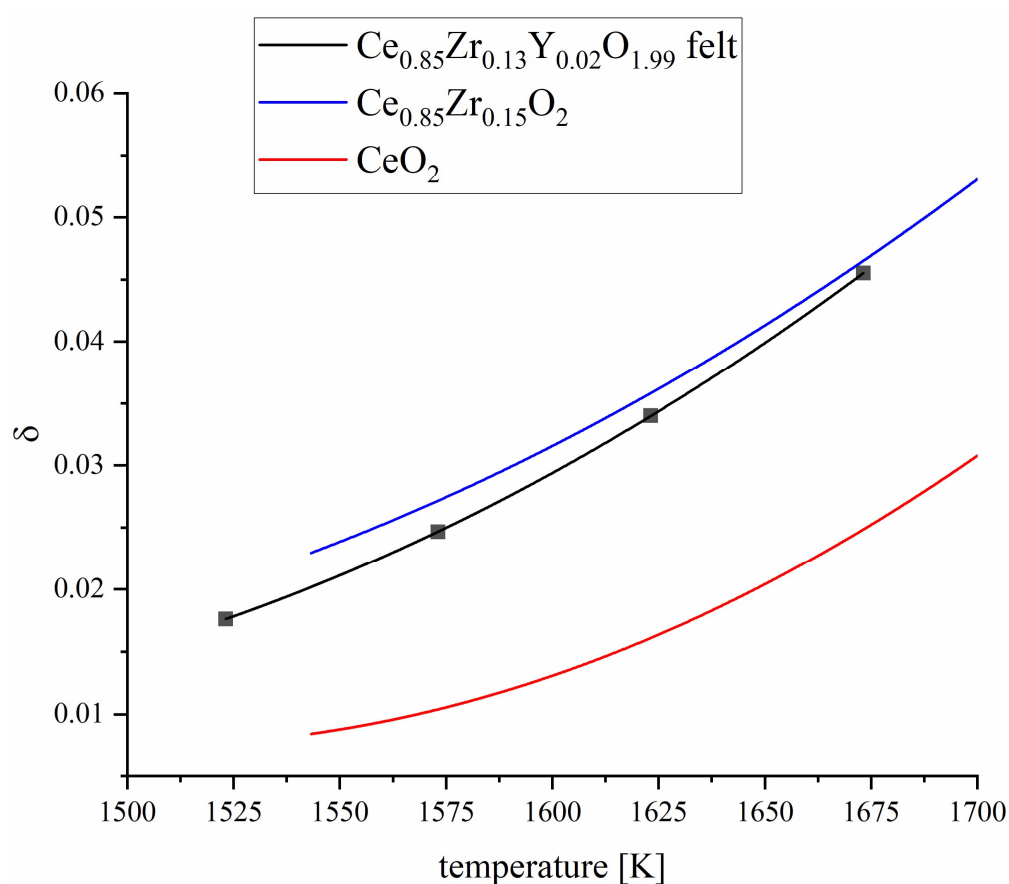


**Figure 12.** Calculated vacancy concentration  $\delta$  of  $\text{Ce}_{0.85}\text{Zr}_{0.13}\text{Y}_{0.02}\text{O}_{1.99}$  in comparison to literature data of  $\text{CeO}_2$  and  $\text{Ce}_{0.85}\text{Zr}_{0.15}\text{O}_2$  measured under the same conditions [51].

Figure 13 shows the re-oxidation curves at 1173 K under air after reduction at 1473 K under Ar (purity of 99,999%). The reduction temperature was chosen so low so that the cooling time to the oxidation temperature is as short as possible.

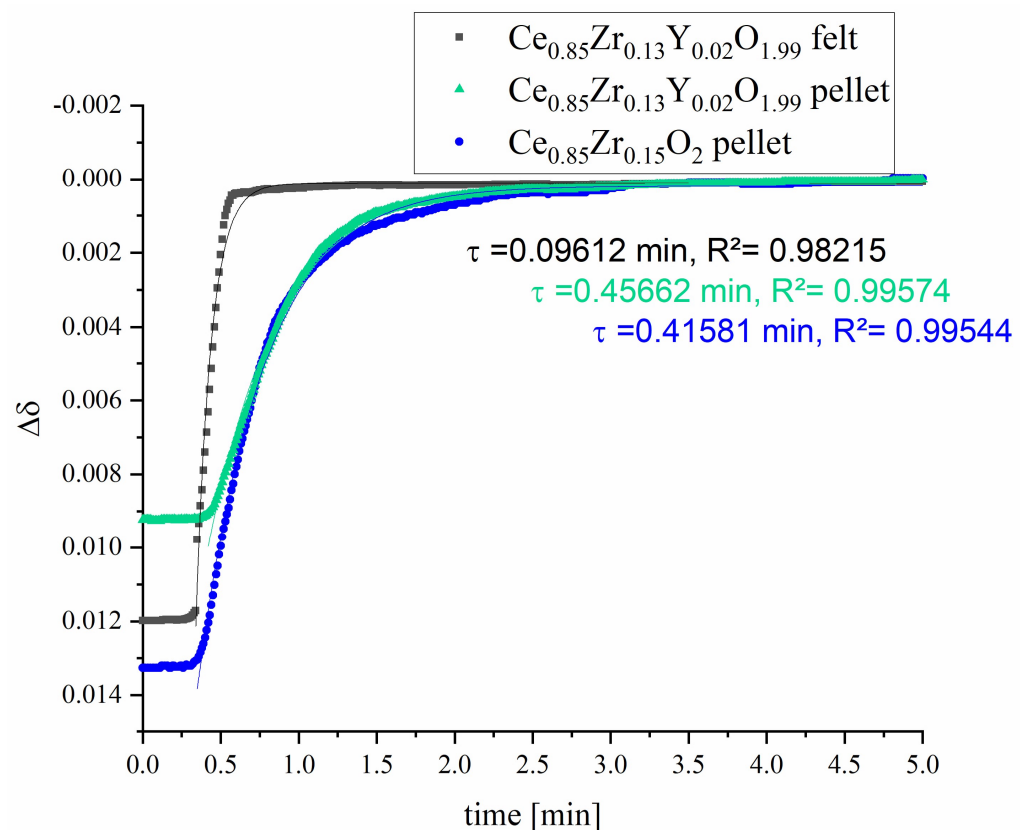


**Figure 13.** Isothermal time dependence of the mass change during re-oxidation at 1173 K of  $\text{Ce}_{0.85}\text{Zr}_{0.13}\text{Y}_{0.02}\text{O}_{1.99}$  felt and pellet in comparison to  $\text{Ce}_{0.85}\text{Zr}_{0.15}\text{O}_2$  pellet [51] after reduction at 1373 K.  $\delta_0$  is the  $\Delta\delta$  at time  $t_0$  when the temperature starts to become constant and the gas is changed from argon to air. Time constants,  $\tau$ , to reach equilibrium are evaluated by fit Equation (4) where the  $R^2$  values quantify the fit quality.

The comparison of the re-oxidation curve of fibrous compacts to curves of dense pellet samples of the same doping and pure Zr doping clearly shows that the re-oxidation rate is many times faster. The mass curves were also fitted by Origin software (OriginLab Inc., Northampton, MA, USA) using the equation

$$y = y_0 + A_1 \exp\left(-\frac{x - x_0}{t_1}\right) \quad (4)$$

which is included in the Origin software as a standard function ('ExpDecay1') for fitting decay-type curves. The calculation of  $t_1$  enables a consideration of the relaxation time constant  $\tau$ . After the time  $t = \ln(2)\tau \approx 0.69\tau$  (half-life), the magnitude has approached half of the final value, after  $t = \tau$  to about 36.8%, after  $t = 2\tau$  to about 13.5%, and after  $t = 3\tau$  to about 5.0%; i.e., the system is relaxed to approx. 95% at this time.

The relaxation time constant of our fibrous compact is much smaller than that of the dense pellets, even though a higher reduction state is present (see Table 1). The use of porous felts can thus result in a significant acceleration of the re-oxidation, which can be attributed to the larger specific surface area and the smaller diffusion paths. Therefore, the fibrous compacts provide both extended reduction and faster re-oxidation kinetics. An early report of a fibrous ceria material shows that a commercial porous ceria felt (CeF-100 by Zircar Zirconia Inc.) with fibers of 7  $\mu\text{m}$  diameter, 100  $\mu\text{m}$  long, 88% porosity and a density of  $0.86 \text{ g cm}^{-3}$  was completely destroyed after cycling using a high flux simulated solar light powered TGA, (reduction and oxidation temperatures of  $\sim 1598 \text{ K}$  and  $\sim 1098 \text{ K}$  for short periods of 4–5 min) due to sintering [38]. Another study of Zr-doped ceria electrospun fibers of 1  $\mu\text{m}$  diameter show a better cycling performance and resistance to sintering up to

1703 K [40]. However, as shown for pure Zr-doped cerium oxide ceramics, higher reduction states can be expected here, but the oxidation rate decreases sharply, leading to slower performance. Our Y-Zr-doped ceria fiber-compacts show fast re-oxidation kinetics and are resistant to high temperature due pre-sintering at 1923 K. The results of X-ray diffraction (Figure 14a) do not give a hint to changes of the structure and further formed phases. The SEM image shows that the fibrous structure is retained even after cycling (Figure 14b). Note that minor remnants of the matrix are visible in this region, but according to EDS analyses their composition is the same as for the fibers.

**Table 1.** Calculated relaxation time constants and reaction times for a turnover of 95% based on the fit of the mass curves in Figure 13 using Equation (4).

Sample	Relaxation Time Constant $\tau$ [min]	t [min] for Turnover of 95%
Ce <sub>0.85</sub> Zr <sub>0.13</sub> Y <sub>0.02</sub> O <sub>1.99</sub> felt	0.09612 ± 0.00121	~0.29
Ce <sub>0.85</sub> Zr <sub>0.13</sub> Y <sub>0.02</sub> O <sub>1.99</sub> pellet	0.45662 ± 0.00289	~1.37
Ce <sub>0.85</sub> Zr <sub>0.15</sub> O <sub>2</sub> pellet	0.41581 ± 0.00268	~1.25

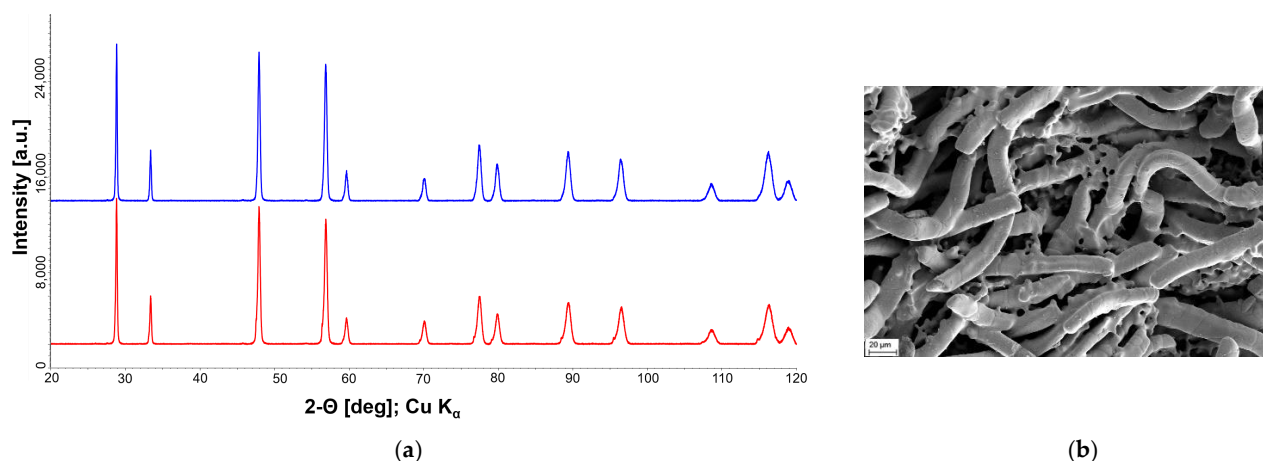


**Figure 14.** (a) XRD-profile of Ce<sub>0.85</sub>Zr<sub>0.13</sub>Y<sub>0.02</sub>O<sub>1.99</sub> felt before (red) and after cycling (blue). (b) SEM of Ce<sub>0.85</sub>Zr<sub>0.13</sub>Y<sub>0.02</sub>O<sub>1.99</sub> felt after cycling.

Furthermore, the thicker nature of the fiber could enable a uniform heating due to deeper penetration and bulk volume absorption of the concentrated solar radiation in comparison to felts described by Pullar et al. [35].

#### 4. Conclusions

Highly porous Ce<sub>0.85</sub>Zr<sub>0.13</sub>Y<sub>0.02</sub>O<sub>1.99</sub> ceramic compacts consisting of fibers with diameters in the range of 8–10 μm have been successfully prepared by infiltration of commercial YSZ fibers with a cerium oxide matrix and subsequent sintering. This preparation technique revealed an unexpected behavior where the cation diffusion is higher at the high dopant concentration side (Y-doped ZrO<sub>2</sub> fibers) and lower at the undoped ceria side. This resulted in quasi unidirectional diffusion and thus complete incorporation of the present ceria matrix into the YSZ fibers. The resulting chemically homogeneous fiber-compacts show strong resistance to sintering and related microstructural degradation. They retain a high porosity of around 58 vol% even after long-term sintering at 1923 K. The fiber-compacts show a high potential for the application in thermochemical redox cycling. The first evaluation of redox kinetics shows that the relaxation time of oxidation is five times faster than that of dense samples of the same composition. The rapid gas exchange due to the high porosity also allows higher reduction rates, which could enable higher hydrogen yields in thermochemical water-splitting redox cycles. The presented fiber-compact prepa-



ration method is considered very promising for cost-effective manufacturing of large-scale functional CeO<sub>2</sub>-based components for solar-thermal high-temperature reactors.

**Author Contributions:** Formal analysis, N.K. and P.M.; Investigation, N.K. and P.M.; Writing—original draft, N.K. and P.M. All authors have read and agreed to the published version of the manuscript.

**Funding:** This research received no external funding.

**Data Availability Statement:** Not applicable.

**Acknowledgments:** Porosity measurements performed by J. Schettler (DLR Institute of Materials Research) are thankfully acknowledged.

**Conflicts of Interest:** The authors declare no conflict of interest.

## References

1. D'Souza, L. Thermochemical hydrogen production from water using reducible oxide materials: A critical review. *Mater. Renew. Sustain. Energy* **2013**, *2*, 1–12. [\[CrossRef\]](#)
2. Roeb, M.; Neises, M.; Monnerie, N.; Call, F.; Simon, H.; Sattler, C.; Schmücker, M.; Pitz-Paal, R. Materials-Related aspects of thermochemical water and carbon dioxide splitting: A review. *Materials* **2012**, *5*, 2015–2054. [\[CrossRef\]](#)
3. Agrafiotis, C.; Roeb, M.; Sattler, C. A review on solar thermal syngas production via redox pair-based water/carbon dioxide splitting thermochemical cycles. *Renew. Sustain. Energy Rev.* **2015**, *42*, 254–285. [\[CrossRef\]](#)
4. Abanades, S.; Flamant, G. Thermochemical hydrogen production from a two-step solar-driven water-splitting cycle based on cerium oxides. *Sol. Energy* **2006**, *80*, 1611–1623. [\[CrossRef\]](#)
5. Chueh, W.C.; Haile, S.M. A thermochemical study of ceria: Exploiting an old material for new modes of energy conversion and CO<sub>2</sub> mitigation. *Philos. Trans. A Math. Phys. Eng. Sci.* **2010**, *368*, 3269–3294. [\[CrossRef\]](#)
6. Knoblauch, N.; Dörrer, L.; Fielitz, P.; Schmücker, M.; Borchardt, G. Surface controlled reduction kinetics of nominally undoped polycrystalline CeO<sub>2</sub>. *Phys. Chem. Chem. Phys.* **2015**, *17*, 5849–5860. [\[CrossRef\]](#) [\[PubMed\]](#)
7. Meng, Q.-L.; Lee, C.; Ishihara, T.; Kaneko, H.; Tamaura, Y. Reactivity of CeO<sub>2</sub>-based ceramics for solar hydrogen production via a two-step water-splitting cycle with concentrated solar energy. *Int. J. Hydrog. Energy* **2011**, *36*, 13435–13441. [\[CrossRef\]](#)
8. Call, F.; Roeb, M.; Schmücker, M.; Bru, H.; Curulla-Ferre, D.; Sattler, C.; Pitz-Paal, R. Thermogravimetric analysis of zirconia-doped ceria for thermochemical production of solar fuel. *AJAC* **2013**, *4*, 37–45. [\[CrossRef\]](#)
9. Kuhn, M.; Bishop, S.R.; Rupp, J.; Tuller, H.L. Structural characterization and oxygen nonstoichiometry of ceria-zirconia (Ce<sub>1-x</sub>Zr<sub>x</sub>O<sub>2-δ</sub>) solid solutions. *Acta Mater.* **2013**, *61*, 4277–4288. [\[CrossRef\]](#)
10. Shah, P.R.; Kim, T.; Zhou, G.; Fornasiero, P.; Gorte, R.J. Evidence for entropy effects in the reduction of ceria–zirconia solutions. *Chem. Mater.* **2006**, *18*, 5363–5369. [\[CrossRef\]](#)
11. Jiang, Q.; Zhou, G.; Jiang, Z.; Li, C. Thermochemical CO<sub>2</sub> splitting reaction with Ce<sub>x</sub>M<sub>1-x</sub>O<sub>2-δ</sub> (M=Ti<sup>4+</sup>, Sn<sup>4+</sup>, Hf<sup>4+</sup>, Zr<sup>4+</sup>, La<sup>3+</sup>, Y<sup>3+</sup> and Sm<sup>3+</sup>) solid solutions. *Sol. Energy* **2014**, *99*, 55–66. [\[CrossRef\]](#)
12. Call, F.; Roeb, M.; Schmücker, M.; Sattler, C.; Pitz-Paal, R. Ceria doped with zirconium and lanthanide oxides to enhance solar thermochemical production of fuels. *J. Phys. Chem. C* **2015**, *119*, 6929–6938. [\[CrossRef\]](#)
13. Scheffe, J.R.; Jacot, R.; Patzke, G.R.; Steinfeld, A. Synthesis, characterization, and thermochemical redox performance of Hf<sup>4+</sup>, Zr<sup>4+</sup>, and Sc<sup>3+</sup> doped ceria for splitting CO<sub>2</sub>. *J. Phys. Chem. C* **2013**, *117*, 24104–24114. [\[CrossRef\]](#)
14. Fornasiero, P.; Kašpar, J.; Graziani, M. On the rate determining step in the reduction of CeO<sub>2</sub>–ZrO<sub>2</sub> mixed oxides. *Appl. Catal. B Environ.* **1999**, *22*, L11–L14. [\[CrossRef\]](#)
15. Yashima, M.; Arashi, H.; Kakihana, M.; Yoshimura, M. Raman scattering study of cubic-tetragonal phase transition in Zr<sub>1-x</sub>Ce<sub>x</sub>O<sub>2</sub> Solid Solution. *J. Am. Ceram. Soc.* **1994**, *77*, 1067–1071. [\[CrossRef\]](#)
16. Le Gal, A.; Abanades, S. Catalytic investigation of ceria-zirconia solid solutions for solar hydrogen production. *Int. J. Hydrog. Energy* **2011**, *36*, 4739–4748. [\[CrossRef\]](#)
17. Le Gal, A.; Abanades, S.; Bion, N.; Le Mercier, T.; Harlé, V. Reactivity of doped ceria-based mixed oxides for solar thermochemical hydrogen generation via two-step water-splitting cycles. *Energy Fuels* **2013**, *27*, 6068–6078. [\[CrossRef\]](#)
18. Shannon, R.D. Revised effective ionic radii and systematic studies of interatomic distances in halides and chalcogenides. *Acta Cryst. A* **1976**, *32*, 751–767. [\[CrossRef\]](#)
19. Kaneko, H.; Taku, S.; Tamaura, Y. Reduction reactivity of CeO<sub>2</sub>–ZrO<sub>2</sub> oxide under high O<sub>2</sub> partial pressure in two-step water splitting process. *Sol. Energy* **2011**, *85*, 2321–2330. [\[CrossRef\]](#)
20. Lemaux, S.; Bensaddik, A.; van der Eerden, A.M.J.; Bitter, J.H.; Koningsberger, D.C. Understanding of enhanced oxygen storage capacity in Ce<sub>0.5</sub>Zr<sub>0.5</sub>O<sub>2</sub>: The presence of an anharmonic pair distribution function in the Zr–O<sub>2</sub> subshell as analyzed by XAFS spectroscopy. *J. Phys. Chem. B* **2001**, *105*, 4810–4815. [\[CrossRef\]](#)
21. Yang, Z.; Woo, T.K.; Hermansson, K. Effects of Zr doping on stoichiometric and reduced ceria: A first-principles study. *J. Chem. Phys.* **2006**, *124*, 224704. [\[CrossRef\]](#) [\[PubMed\]](#)

22. Rodriguez, J.A.; Hanson, J.C.; Kim, J.-Y.; Liu, G.; Iglesias-Juez, A.; Fernández-García, M. Properties of CeO<sub>2</sub> and Ce<sub>1-x</sub>Zr<sub>x</sub> nanoparticles: X-ray absorption near-edge spectroscopy, density functional, and time-resolved X-ray diffraction studies. *J. Phys. Chem. B* **2003**, *107*, 3535–3543. [[CrossRef](#)]
23. Wang, H.-F.; Guo, Y.-L.; Lu, G.-Z.; Hu, P. Maximizing the localized relaxation: The origin of the outstanding oxygen storage capacity of kappa-Ce<sub>2</sub>Zr<sub>2</sub>O<sub>8</sub>. *Angew. Chem. Int. Ed. Engl.* **2009**, *48*, 8289–8292. [[CrossRef](#)]
24. Zhou, G.; Shah, P.R.; Kim, T.; Fornasiero, P.; Gorte, R.J. Oxidation entropies and enthalpies of ceria–zirconia solid solutions. *Catal. Today* **2007**, *123*, 86–93. [[CrossRef](#)]
25. Le Gal, A.; Abanades, S.; Flamant, G. CO<sub>2</sub> and H<sub>2</sub>O splitting for thermochemical production of solar fuels using nonstoichiometric ceria and ceria/zirconia solid solutions. *Energy Fuels* **2011**, *25*, 4836–4845. [[CrossRef](#)]
26. Hao, Y.; Yang, C.-K.; Haile, S.M. Ceria–Zirconia solid solutions (Ce<sub>1-x</sub>Zr<sub>x</sub>O<sub>2-δ</sub>, x ≤ 0.2) for solar thermochemical water splitting: A thermodynamic study. *Chem. Mater.* **2014**, *26*, 6073–6082. [[CrossRef](#)]
27. Abanades, S.; Legal, A.; Cordier, A.; Peraudeau, G.; Flamant, G.; Julbe, A. Investigation of reactive cerium-based oxides for H<sub>2</sub> production by thermochemical two-step water-splitting. *J. Mater. Sci.* **2010**, *45*, 4163–4173. [[CrossRef](#)]
28. Le Gal, A.; Abanades, S. Dopant incorporation in ceria for enhanced water-splitting activity during solar thermochemical hydrogen generation. *J. Phys. Chem. C* **2012**, *116*, 13516–13523. [[CrossRef](#)]
29. Rudisill, S.G.; Venstrom, L.J.; Petkovich, N.D.; Quan, T.; Hein, N.; Boman, D.B.; Davidson, J.H.; Stein, A. Enhanced oxidation kinetics in thermochemical cycling of CeO<sub>2</sub> through templated porosity. *J. Phys. Chem. C* **2013**, *117*, 1692–1700. [[CrossRef](#)]
30. Eufinger, J.-P.; Daniels, M.; Schmale, K.; Berendts, S.; Ulbrich, G.; Lerch, M.; Wiemhöfer, H.-D.; Janek, J. The model case of an oxygen storage catalyst—non-stoichiometry, point defects and electrical conductivity of single crystalline CeO<sub>2</sub>–ZrO<sub>2</sub>–Y<sub>2</sub>O<sub>3</sub> solid solutions. *Phys. Chem. Chem. Phys.* **2014**, *16*, 25583–25600. [[CrossRef](#)]
31. Vidmar, P.; Fornasiero, P.; Kašpar, J.; Gubitosa, G.; Graziani, M. Effects of trivalent dopants on the redox properties of Ce<sub>0.6</sub>Zr<sub>0.4</sub>O<sub>2</sub> mixed oxide. *J. Catal.* **1997**, *171*, 160–168. [[CrossRef](#)]
32. Yahiro, H.; Eguchi, Y.; Eguchi, K.; Arai, H. Oxygen ion conductivity of the ceria-samarium oxide system with fluorite structure. *J. Appl. Electrochem.* **1988**, *18*, 527–531. [[CrossRef](#)]
33. Qi, X.; Lin, Y.S.; Holt, C.T.; Swartz, S.L. Electric conductivity and oxygen permeability of modified cerium oxides. *J. Mater. Sci.* **2003**, *38*, 1073–1079. [[CrossRef](#)]
34. Grieshammer, S. Defect interactions in the CeO<sub>2</sub>–ZrO<sub>2</sub>–Y<sub>2</sub>O<sub>3</sub> solid solution. *J. Phys. Chem. C* **2017**, *121*, 15078–15084. [[CrossRef](#)]
35. Pullar, R.C.; Novais, R.M.; Caetano, A.P.F.; Barreiros, M.A.; Abanades, S.; Oliveira, F.A.C. A review of solar thermochemical CO<sub>2</sub> splitting using ceria-based ceramics with designed morphologies and microstructures. *Front. Chem.* **2019**, *7*, 601. [[CrossRef](#)] [[PubMed](#)]
36. Furler, P.; Scheffe, J.; Gorb, M.; Moes, L.; Vogt, U.; Steinfeld, A. Solar thermochemical CO<sub>2</sub> splitting utilizing a reticulated porous ceria redox system. *Energy Fuels* **2012**, *26*, 7051–7059. [[CrossRef](#)]
37. Furler, P.; Scheffe, J.R.; Steinfeld, A. Syngas production by simultaneous splitting of H<sub>2</sub>O and CO<sub>2</sub> via ceria redox reactions in a high-temperature solar reactor. *Energy Environ. Sci.* **2012**, *5*, 6098–6103. [[CrossRef](#)]
38. Takacs, M.; Ackermann, S.; Bonk, A.; Neises-von Puttkamer, M.; Haueter, P.; Scheffe, J.R.; Vogt, U.F.; Steinfeld, A. Splitting CO<sub>2</sub> with a ceria-based redox cycle in a solar-driven thermogravimetric analyzer. *AIChE J.* **2017**, *63*, 1263–1271. [[CrossRef](#)] [[PubMed](#)]
39. Gladen, A.C.; Davidson, J.H. The morphological stability and fuel production of commercial fibrous ceria particles for solar thermochemical redox cycling. *Sol. Energy* **2016**, *139*, 524–532. [[CrossRef](#)]
40. Gibbons, W.T.; Venstrom, L.J.; de Smith, R.M.; Davidson, J.H.; Jackson, G.S. Ceria-Based electrospun fibers for renewable fuel production via two-step thermal redox cycles for carbon dioxide splitting. *Phys. Chem. Chem. Phys.* **2014**, *16*, 14271–14280. [[CrossRef](#)]
41. Bishop, S.R. Chemical expansion of solid oxide fuel cell materials: A brief overview. *Acta. Mech. Sin.* **2013**, *29*, 312–317. [[CrossRef](#)]
42. Crank, J. *The Mathematics of Diffusion*, 2nd ed.; Oxford University Press: London, UK, 1975; ISBN 0-19-853344-6.
43. Beschnitt, S.; de Souza, R.A. Impurity diffusion of Hf and Zr in Gd-doped CeO<sub>2</sub>. *Solid State Ion.* **2017**, *305*, 23–29. [[CrossRef](#)]
44. Zhang, Y.; Li, J.; Li, Q.; Zhu, L.; Liu, X.; Zhong, X.; Meng, J.; Cao, X. Preparation of CeO<sub>2</sub>–ZrO<sub>2</sub> ceramic fibers by electrospinning. *J. Colloid Interface Sci.* **2007**, *307*, 567–571. [[CrossRef](#)]
45. Dong, Y.; Wang, C.-A.; Zhou, J. Effect of YSZ fiber addition on microstructure and properties of porous YSZ ceramics. *J. Mater. Sci.* **2012**, *47*, 6326–6332. [[CrossRef](#)]
46. Hu, L.; Wang, C.-A.; Huang, Y. Porous yttria-stabilized zirconia ceramics with ultra-low thermal conductivity. *J. Mater. Sci.* **2010**, *45*, 3242–3246. [[CrossRef](#)]
47. Darcy, H. *Les Fontaines Publiques de la Ville de Dijon*; Victor Dalmont: Paris, France, 1856.
48. Kawagoe, Y.; Oshima, T.; Tomarikawa, K.; Tokumasu, T.; Koido, T.; Yonemura, S. A study on pressure-driven gas transport in porous media: From nanoscale to microscale. *Microfluid. Nanofluid.* **2016**, *20*. [[CrossRef](#)]
49. Haussener, S.; Steinfeld, A. Effective heat and mass transport properties of anisotropic porous ceria for solar thermochemical fuel generation. *Materials* **2012**, *5*, 192–209. [[CrossRef](#)]
50. Isobe, T.; Kameshima, Y.; Nakajima, A.; Okada, K.; Hotta, Y. Gas permeability and mechanical properties of porous alumina ceramics with unidirectionally aligned pores. *J. Eur. Ceram. Soc.* **2007**, *27*, 53–59. [[CrossRef](#)]
51. Knoblauch, N. Synthese, Charakterisierung und Untersuchung zum Redoxverhalten von ceroxidbasierten Materialien zur Erzeugung Solarer Brennstoffe. Ph.D. Thesis, Technische Universität Clausthal, Clausthal-Zellerfeld, Germany, 2018. [[CrossRef](#)]